

Supplementary Materials for

Carbon-boron clathrates as a new class of sp^3 -bonded framework materials

Li Zhu, Gustav M. Borstad, Hanyu Liu, Piotr A. Guńka, Michael Guerette, Juli-Anna Dolyniuk, Yue Meng, Eran Greenberg, Vitali B. Prakapenka, Brian L. Chaloux, Albert Epshteyn, Ronald E. Cohen, Timothy A. Strobel*

*Corresponding author. Email: tstrobel@carnegiescience.edu

Published 10 January 2020, *Sci. Adv.* **6**, eaay8361 (2020)
DOI: 10.1126/sciadv.aay8361

The PDF file includes:

Single-crystal diffraction analysis

Fig. S1. Stability of SrB_3C_3 and analysis of different possible stoichiometries.

Fig. S2. SEM and EDS measurements.

Fig. S3. Raw XRD patterns.

Fig. S4. Sr-B-C phase identification.

Fig. S5. Optical images of SrB_3C_3 during synthesis near 50 GPa.

Fig. S6. Electronic structures for SrB_3C_3 .

Fig. S7. Phonon dispersion curves and energetic stabilities as a function of pressure.

Fig. S8. Fourier difference map ($F_{obs} - F_{calc}$) from single-crystal analysis.

Table S1. Comparison of single-crystal diffraction refinement quality indicators for different “colorings” of clathrate framework in crystal structure models of the SrB_3C_3 clathrate.

Table S2. Calculated Bader partial charges of the SrB_3C_3 clathrate at 0 GPa.

Table S3. Calculated structural parameters of Sr-B-C phases.

Table S4. SrB_3C_3 lattice parameters during decompression.

Other Supplementary Material for this manuscript includes the following:

(available at advances.sciencemag.org/cgi/content/full/6/2/eaay8361/DC1)

Data file S1. CIF file of the single-crystal XRD data and the best model of the crystal structure for the SrB_3C_3 clathrate.

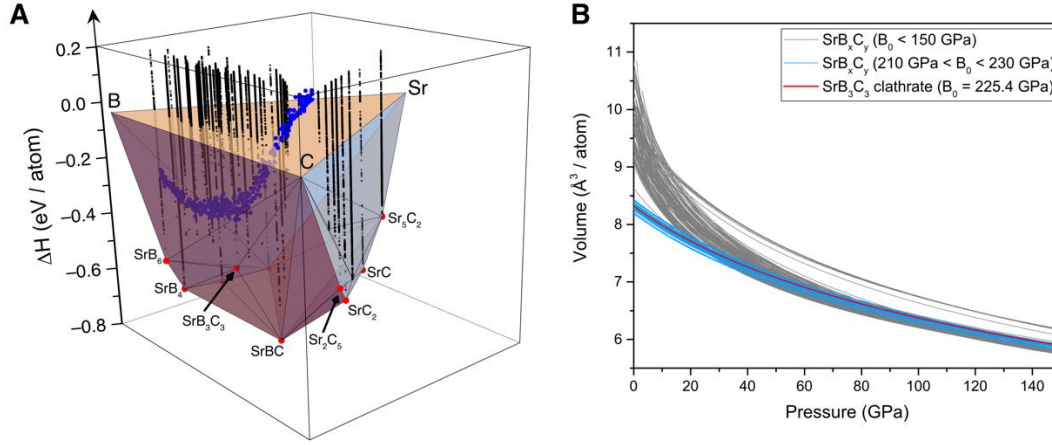


Fig. S1. Stability of SrB_3C_3 and analysis of different possible stoichiometries. (A) Predicted formation enthalpies of various Sr-B-C compounds with respect to elemental decomposition at 50 GPa. Compounds with enthalpy data represented by red points are on the convex hull and thermodynamically stable against decomposition. Black points show the formation enthalpies of metastable structures found in the CALYPSO structure searches. Blue points above the convex hull indicate the formation enthalpies of 600 additional structures containing up to 112 atoms with compositions SrB_xC_y (excluding SrB_3C_3). These 600 structures were determined from searches wherein the Sr^{2+} cations were constrained to a tolerance within the experimentally determined cubic positions, while the ratio and positions of C and B atoms were allowed to freely fluctuate. No composition was found to be more stable than SrB_3C_3 and no other composition is on the convex hull. (B) The calculated EoS of the 600 SrB_xC_y compounds presented in A. The red line shows the EoS of SrB_3C_3 clathrate, which agrees with experiment. The grey lines represent the EoS of different SrB_xC_y compounds with calculated $B_0 < 150$ GPa, while the cyan lines indicate the structures with calculated B_0 in the range of 210 to 230 GPa. After a careful analysis, we found that all of the structures from the cyan group can be classified as type-VII clathrate structures (*e.g.*, 4^66^8 cages with different B:C compositions) whereas structures from the grey group are not cage-like structures and are more compressible. As the experimental EoS is located in the cyan group and SrB_3C_3 is the lowest energy structure determined, the synthesized product is only consistent with a clathrate structure that should be identical or similar to the structure of cubic SrB_3C_3 .

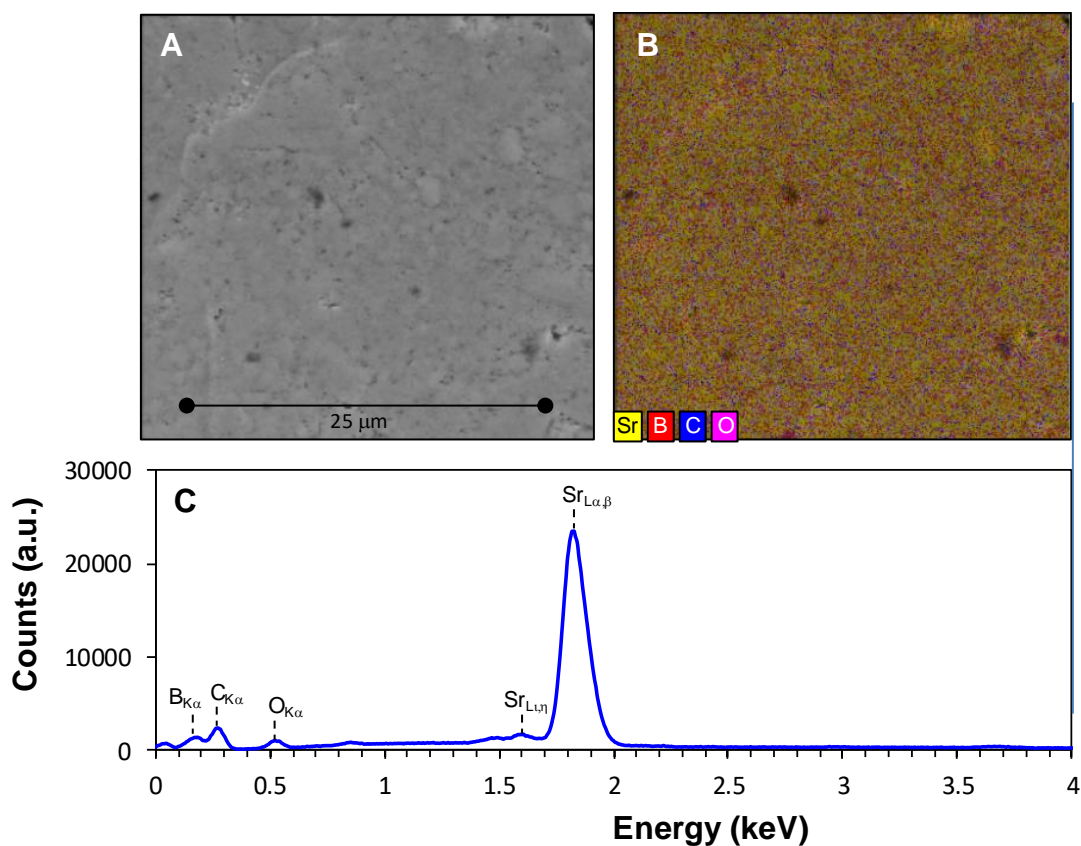


Fig. S2. SEM and EDS measurements. High-resolution EDS mapping was performed on a $\sim 30 \times 30 \mu\text{m}^2$ area in the central region of the laser-heated sample subsequent to synchrotron XRD measurements, which confirmed the cubic diffraction pattern attributed to SrB_3C_3 . The region exhibits an overall uniform elemental distribution with no evidence for phase segregation. The average composition was determined to be $\text{Sr}_{1 \pm 0.07} \text{B}_{3.86 \pm 0.23} \text{C}_{4.62 \pm 0.18} \text{O}_{0.40 \pm 0.05}$. The small oxygen content is attributed to minor surface oxidation during the sample transfer, and excess carbon is attributed to adventitious sources, also observed on the surface of pure silicon wafer standards.

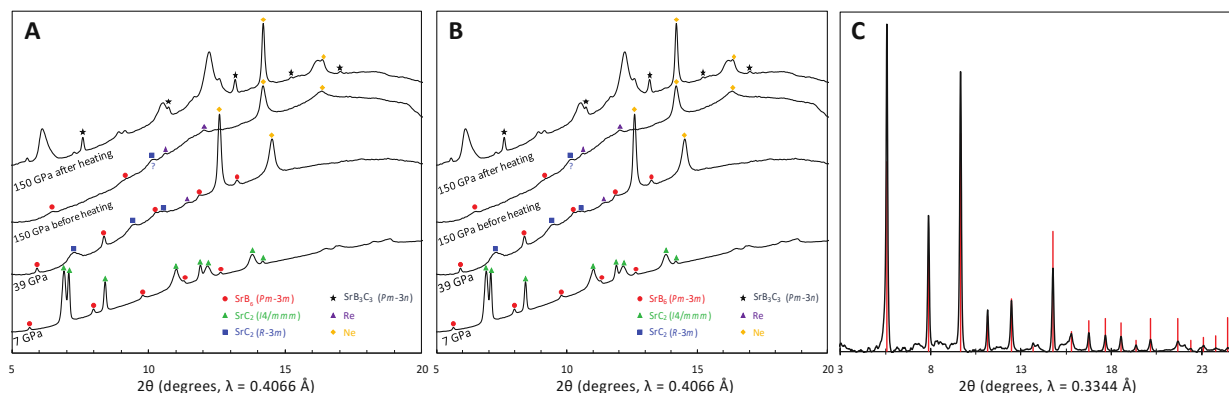


Fig. S3. Raw XRD patterns. (A) The starting material is a mixture of SrB_6 ($Pm\bar{3}m$), SrC_2 ($I4/mmm$) and glassy C in a 1:1:4 molar ratio, e.g., 2Sr:6C:6B. SrC_2 and glassy carbon appear to be amorphous to X-rays and are not distinguishable from crystalline SrB_6 . After heating to a maximum temperature of ~ 2900 K, the stoichiometric 1Sr:3C:3B mixture was converted to nearly phase-pure SrB_3C_3 with trace residual SrB_6 . (B) The starting material is a mixture of SrB_6 ($Pm\bar{3}m$) and SrC_2 ($I4/mmm$) in a 1:3 molar ratio. Above 14 GPa, SrC_2 transforms to the $R\bar{3}m$ structure. All Bragg peaks broaden significantly and diminish in intensity with pressure due to significant stress accumulation prior to heating. Above *ca.* 50 GPa, SrC_2 appears to become amorphous to X-rays; one broad feature is potentially attributable to the $R\bar{3}m$ phase. After heating at ~ 150 GPa, many new Bragg peaks appear, which can be attributed to SrB_3C_3 , SrBC and a high-pressure form of SrB_6 , as described below. (C) X-ray diffraction of SrB_3C_3 at atmospheric pressure. After synthesis at ~ 57 GPa, the cell was decompressed, the neon gas was released and XRD patterns were collected after the cell was sealed at 1 atm. The refined lattice parameter of $a = 4.868$ Å compares well with DFT-GGA calculations where $a = 4.88$ Å. Red bars indicate calculated positions for the cubic clathrate structure. When left in open air, SrB_3C_3 appears to degrade and is thus sensitive to moisture and/or oxygen.

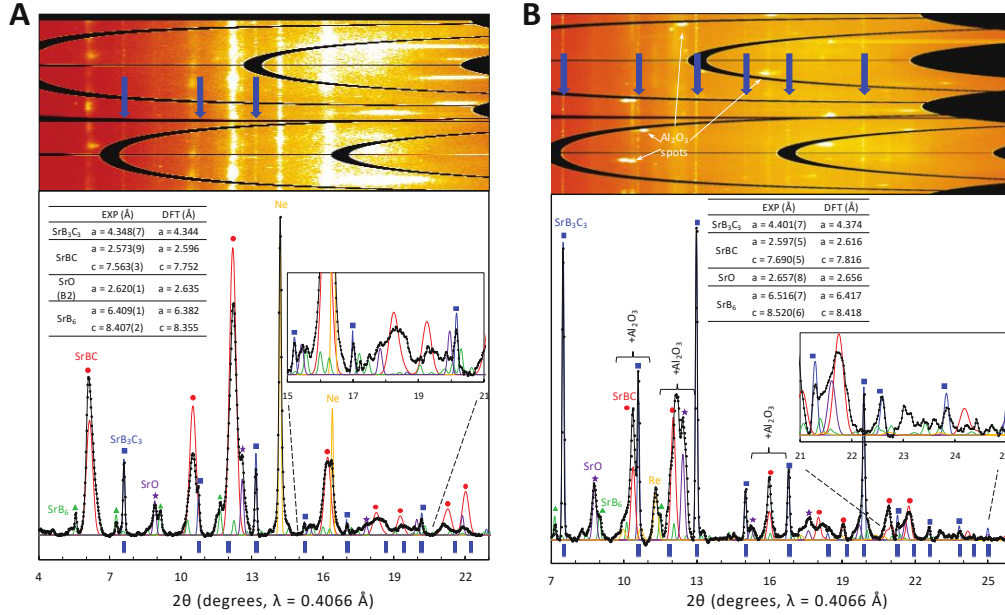


Fig. S4. Sr-B-C phase identification. (A) Sr-B-C phase identification at 155(6) GPa with Ne medium. The starting material is a mixture of SrB₆ ($Pm\bar{3}m$) and SrC₂ ($I4/mmm$) in a 1:3 molar ratio. The data indicate the reaction $\text{SrB}_6 + 3\text{SrC}_2 \rightarrow \text{SrB}_3\text{C}_3 + 3\text{SrBC}$ (and some unconverted SrB₆ in a high-pressure phase), which is calculated to be the most energetically favorable reaction for these conditions. Experimental data are shown as black points connected by a thin black line. Each phase is labeled with a different symbol; tick marks below the pattern indicate allowed reflections for SrB₃C₃ ($Pm\bar{3}n$). Rietveld refinement was conducted using only a Gaussian peak width and scale parameter. All atomic positions were taken from DFT-optimized structures shown in the tables below. Powder averaging statistics vary between phases. Experimentally refined lattice parameters are compared with DFT (PBE) optimizations at 155 GPa. The inset to the right shows quantitative intensity agreement for SrB₃C₃ to the limiting resolution of $d = 1.16$ Å. The 2D cake image is presented at the top of the figure with arrows indicating prominent sharp lines for SrB₃C₃. (B) Sr-B-C phase identification at 142(10) GPa with Al₂O₃ medium. The starting material is a mixture of SrB₆ ($Pm\bar{3}m$) and SrC₂ ($I4/mmm$) in a 1:3 molar ratio. The data indicate the reaction $\text{SrB}_6 + 3\text{SrC}_2 \rightarrow \text{SrB}_3\text{C}_3 + 3\text{SrBC}$ (and some unconverted SrB₆ in a high-pressure phase), which is calculated to be the most energetically favorable reaction for these conditions. Experimental data are shown as black points connected by a thin black line. Each phase is labeled with a different symbol; tick marks below the pattern indicate allowed reflections for SrB₃C₃ ($Pm\bar{3}n$). Rietveld refinement was conducted using only a Gaussian peak width and scale parameter. All atomic positions were taken from DFT-optimized structures shown in the table below. Powder averaging statistics vary between phases. Experimentally refined lattice parameters are compared with DFT (PBE) optimizations at 140 GPa. The inset to the right shows quantitative intensity agreement for SrB₃C₃ to the limiting resolution of $d = 0.93$ Å. The 2D cake image is presented at the top of the figure with arrows indicating prominent sharp lines for SrB₃C₃. Strong single-crystalline Al₂O₃ peaks were masked, but some powder intensity was unavoidable due to the breaking of crystals during compression to 140 GPa.

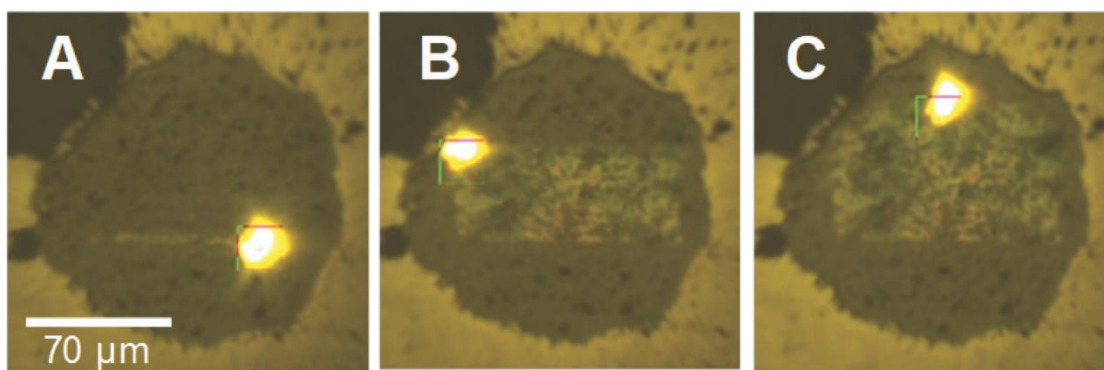


Fig. S5. Optical images of SrB_3C_3 during synthesis near 50 GPa. As the heating laser (bright yellow spot) passes across the sample (from A to C), the starting material is converted to SrB_3C_3 , which exhibits a metallic luster.

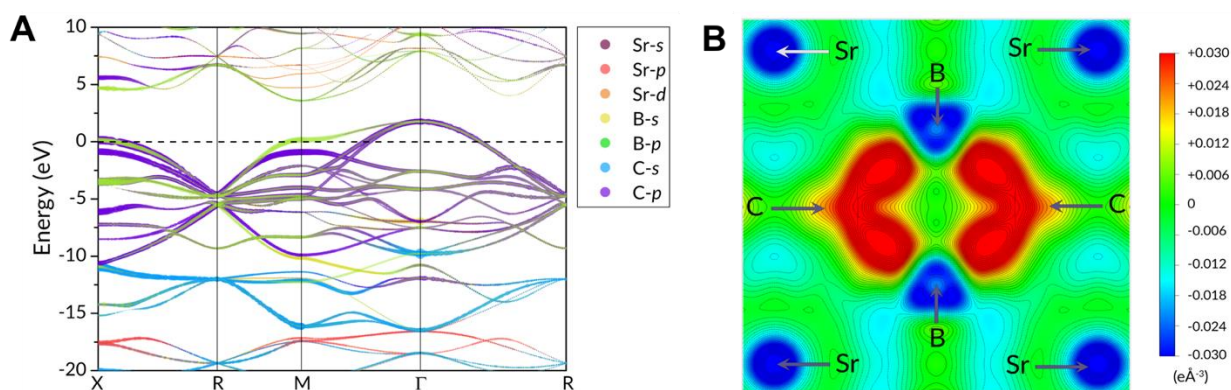


Fig. S6. Electronic structures for SrB_3C_3 . (A) Electronic structures for SrB_3C_3 at 200 GPa projected onto atomic orbitals represented by different colors. The width of each band is proportional to the weight of the corresponding orbital character. The dashed line indicates the Fermi energy. (B) Difference charge density (crystal density minus superposition of isolated atomic densities) of SrB_3C_3 plotted in the (100) plane at 0 GPa. Arrows denote the positions of Sr, B, and C atoms, as indicated.

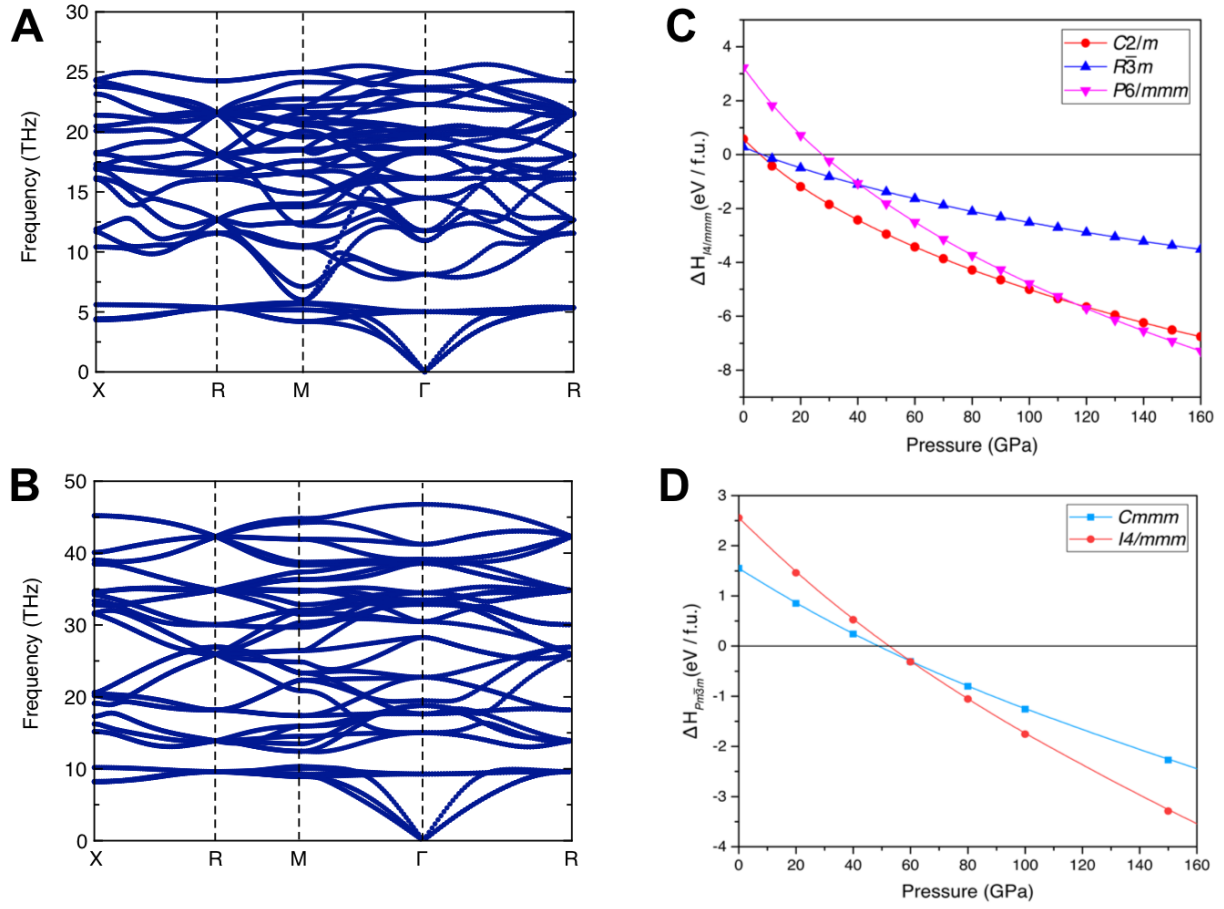


Fig. S7. Phonon dispersion curves and energetic stabilities as a function of pressure. Phonon dispersion curves for SrB_3C_3 at 0 GPa (A) and 200 GPa (B). The absence of any imaginary frequency in the entire Brillouin zone demonstrates the dynamical stability of the SrB_3C_3 clathrate. (C) Calculated enthalpies (H) per SrC_2 unit as a function of pressure for various structures with respect to $I4/mmm$ structure. (D) Calculated enthalpies (H) per SrB_6 unit as a function of pressure for various structures with respect to $Pm\bar{3}m$ structure.

Single-crystal diffraction analysis

Prolonged double-sided laser heating of a powder sample at ~3000 K and 56(4) GPa led to its recrystallization and formation of multiple relatively large grains suitable for multigrain analysis. An omega scan was carried out over the cell-limited range from -16° to 18° and images were recorded using PILATUS 1M-F detector every 0.5° with an exposure time of 0.5 s. The diffraction patterns were analyzed using the Fable package. High intensity peaks harvested using the ImageD11 program were indexed with GrainSpotter. This procedure produced two grains with distinct orientation matrices. Subsequently, reflections coming from the two grains were manually integrated using GSE_ADA/RSV software package. Reflections with intensity significantly deviating from the average intensity of their symmetry equivalents were removed from the data sets manually. It is noteworthy that the intensity of the $\{120\}$ reflections was significantly different from zero with $I/\sigma(I)$ around 15 (for four measured symmetry equivalents) which indicates that SrC_3B_3 crystallises in a primitive cubic cell and not a BCC cell (in which case hkl reflections only have non-zero intensity if $h + k + l = 2n$). Crystal structure determination was performed with the integrated data, and it was determined that the data coming from one of the grains were significantly better than from the other one. The final model was refined against reflections from the first grain only with only one scaled reflection from the other grain which was not recorded for the first grain. The crystal structure was solved by direct methods in the $Pm\bar{3}n$ space group using SHELXS and refined by least-squares minimizations using SHELXL-2014. Both programs were invoked from within the Olex2 suite. The difference maps of a model containing only Sr^{2+} cations atoms at the $2a$ Wyckoff position exhibited highest peaks at the $6c$ and $6d$ sites confirming the presence of clathrate framework in the crystal (Figure S8). Carbon and boron atoms were placed in these positions and we found that there are differences between all-carbon, all-boron and mixed carbon-boron structural models. The bipartite model with both carbon and boron atoms exhibits the best R_I value (see Table S1 for quality indicators for different models). Due to the low data completeness and, consequently, low data-to-parameter ratio, only one free variable for the isotropic displacement parameters of all atoms in the asymmetric unit was used. While it can be argued that the quality of the collected diffraction data does not permit for an unequivocal determination of the clathrate framework “coloring” (boron-carbon arrangement on the lattice), the data do confirm the presence of the clathrate framework in the crystal and fully corroborate the predicted SrB_3C_3 crystal structure. The single-crystal XRD data and the best model of the crystal structure are provided in the supplemental CIF file.

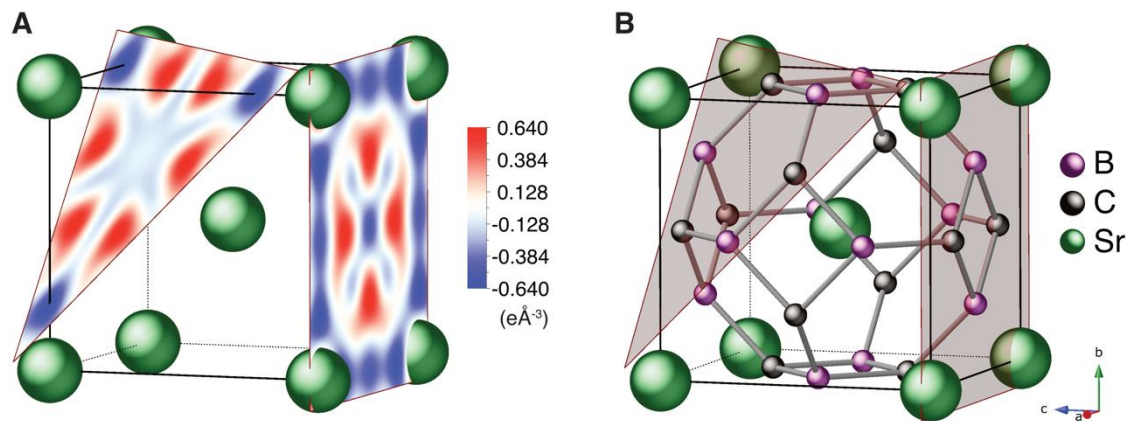


Fig. S8. Fourier difference map ($F_{\text{obs}} - F_{\text{calc}}$) from single-crystal analysis. After determination of the Sr^{2+} cations at the $2a$ Wyckoff position, clear residual electron density (A) is observed at the $6c$ and $6d$ positions, unambiguously indicating the presence of the clathrate framework in the structural model (B).

Table S1. Comparison of single-crystal diffraction refinement quality indicators for different “colorings” of clathrate framework in crystal structure models of the SrB_3C_3 clathrate.

	Model 0	Model 1	Model 2	Model 3
Atom positions	Sr ($2a$) - ($6c$) - ($6d$)	Sr ($2a$) B ($6c$) C ($6d$)	Sr ($2a$) C ($6c$) C ($6d$)	Sr ($2a$) B ($6c$) B ($6d$)
Reflections collected	16 ($R_{\text{int}} = 0.0586$, $R_{\text{sigma}} = 0.0400$)			
Independent reflections	7			
Data/restraints/parameters	7/0/2			
$U_{\text{iso}}(\text{Sr, B, C})$	0.01(3)	0.013(6)	0.010(6)	0.007(6)
Goodness-of-fit on F^2	3.387	1.444	1.346	1.235
Final R indexes [$I \geq 2\sigma(I)$]	$R_1 = 0.2128$, $wR_2 = 0.5609$	$R_1 = 0.0504$, $wR_2 = 0.1387$	$R_1 = 0.0631$, $wR_2 = 0.1229$	$R_1 = 0.0625$, $wR_2 = 0.1357$
Final R indexes [all data]	$R_1 = 0.2175$, $wR_2 = 0.5743$	$R_1 = 0.0518$, $wR_2 = 0.1422$	$R_1 = 0.0687$, $wR_2 = 0.1253$	$R_1 = 0.0681$, $wR_2 = 0.1377$
Largest diff. peak/hole / $\text{e}\text{\AA}^{-3}$	+3.47/−4.90	+0.79/−0.65	+0.49/−0.56	+0.81/−0.93

Table S2. Calculated Bader partial charges of the SrB₃C₃ clathrate at 0 GPa. The electrons are transferred from the Sr atoms to the B-C cage. Polar covalent bonds are formed because of the different electronegativities between the B and C atoms. B has an electronegativity of 2.04 on the Pauling scale lower than the value for C (2.55), and the nature of polar covalent bonding is also demonstrated by the difference charge density (Fig. S6).

Atom	Partial charge
Sr	+1.35
B	+1.48
C	-1.93

Table S3. Calculated structural parameters of Sr-B-C phases.

	Space group	Pressure (GPa)	Lattice Parameters (Å, °)	Atomic coordinates (fractional)			
				Atom	X	Y	Z
SrB ₃ C ₃	$Pm\bar{3}n$	0	a = 4.884	Sr (2a)	0	0	0
				B (6c)	¼	0	½
				C (6d)	¼	½	0
SrBC	$P6_3/mmc$	0	a = 3.023	Sr (2a)	0	0	0
			c = 8.996	B (2d)	⅓	⅔	¾
				C (2d)	⅓	⅔	¼
SrB ₆	$Pm\bar{3}m$	0	a = 4.198	Sr (1a)	0	0	0
				B (6f)	0.797	½	½
SrB ₆	$Cmcm$	60	a = 6.643	Sr (4i)	0	0.296	0
			b = 8.352	B (4h)	0.619	0	½
			c = 3.835	B (4j)	0	0.094	½
				B (8q)	0.225	0.159	½
				B (8o)	0.812	0	0.791
SrB ₆	$I4/mmm$	150	a = 6.382	Sr (4d)	0	½	¼
			c = 8.375	Sr (4e)	0	0	0.160
				B (16l)	0.680	0.127	0
				B (16m)	0.773	0.773	0.340
				B (16n)	0	0.805	0.408
SrC ₂	$I4/mmm$	0	a = 4.114	Sr (2a)	0	0	0
			c = 6.832	B (4e)	0	0	0.408
SrC ₂	$R\bar{3}m$	10	a = 3.542	Sr (1a)	0	0	0
			α = 83.7	C (2c)	0.407	0.407	0.407
SrC ₂	$C2/m$	60	a = 8.201	Sr (4i)	0.318	0	0.890
			b = 5.533	Sr (4i)	0.704	0	0.614
			c = 5.725	C (4i)	0.978	0	0.107
			β = 116.8	C (4h)	0	0.872	½
				C (8j)	0.009	0.219	0.741
SrC ₂	$P6/mmm$	150	a = 2.554	Sr (1a)	0	0	0
			b = 3.873	C (2d)	⅓	⅔	½

Table S4. SrB₃C₃ lattice parameters during decompression.

Cell #1 – Ne medium

Synthesis: ~55 GPa at ≤ 2900 K

P (GPa)	a (Å)
57(3)	4.590
55(3)	4.606
49(2)	4.634
46(2)	4.644
45(2)	4.656
42(2)	4.664
37(2)	4.688
33(2)	4.702
29(1)	4.720
26(1)	4.746
0.0(2)	4.868

Cell #2 – Ne medium

Synthesis: 63 GPa at ≤ 2900 K

P (GPa)	a (Å)
63(3)	4.576(4)
57(2)	4.615(7)
56(2)	4.626(6)
55(2)	4.633(7)
52(2)	4.645(8)
47(2)	4.662(5)
44(2)	4.670(6)
43(2)	4.664(7)
40(2)	4.682(6)
38(2)	4.685(7)
35(1)	4.692(6)
32(1)	4.701(8)
31(1)	4.706(9)
27(1)	4.741(4)
24(1)	4.750(5)
21(1)	4.781(9)
7.3(3)	4.843(6)
5.8(2)	4.847(8)
5.2(2)	4.854(4)
4.7(2)	4.847(4)

Cell #3 – Ne medium
Synthesis: ~115 GPa at
 $\leq 2900\text{ K}$

P (GPa)	a (Å)
114(4)	4.453(5)

Cell #4 – Ne medium
Synthesis: ~155 GPa at
 $\leq 2500\text{ K}$

P (GPa)	a (Å)
156(7)	4.373(5)

Cell #5 – Ne medium
Synthesis: ~160 GPa at
 $\leq 2200\text{ K}$

P (GPa)	a (Å)
161(7)	4.341(3)
150(6)	4.363(2)
147(6)	4.370(2)
143(6)	4.377(2)
139(6)	4.386(4)
134(5)	4.405(3)
130(5)	4.416(3)
126(5)	4.425(4)
122(5)	4.447(11)
116(5)	4.444(5)
111(4)	4.455(3)
103(4)	4.474(2)
90(4)	4.521(8)
77(3)	4.561(7)

Cell #6 – Al₂O₃ medium
Synthesis: ~140 GPa at
≤2800 K

P (GPa)	a (Å)
142(10)	4.4014(3)
138(10)	4.4098(6)
136(10)	4.4155(5)
136(9)	4.4224(7)
133(9)	4.426(1)
125(9)	4.442(2)
126(9)	4.433(2)
110(8)	4.479(2)
96(7)	4.513(2)
64(4)	4.584(3)
22(4)	4.738(2)